



Research Paper

Computational modeling of evaporation without tuning coefficients

Ayaaz Yasin ^{a,b}, Kishan Bellur ^b*^a Department of Aerospace Engineering and Engineering Mechanics, University of Cincinnati, Cincinnati, OH 45220, USA^b Department of Mechanical and Materials Engineering, University of Cincinnati, Cincinnati, OH 45220, USA

ARTICLE INFO

Keywords:

Evaporation
Accommodation coefficient
Kinetic theory
Computational fluid dynamics
Hydrogen
Methane

ABSTRACT

Evaporation is omnipresent in both natural phenomena and engineered devices. Although recent studies have progressed our understanding of phase change physics, reliable models to compute interphase mass and heat transfer remain elusive. Popular models, such as Lee's model, rely heavily on tuning coefficients that are not universal, posing a significant challenge in many fields. In this work, these challenges are addressed through a novel computational approach that uniquely combines kinetic theory of phase change, transition state theory and CFD. A new computational routine capable of modeling phase change without tuning parameters or coefficient inputs is presented. Vapor temperature is found to play a critical role in the accurate prediction of phase change rates. Kinetic models require vapor temperature from within the Knudsen layer as inputs to accurately model evaporation rates. Due to the inability of CFD models to capture temperature gradients in the Knudsen layer, a new parameter, γ , is introduced to approximate the Knudsen layer vapor temperature. The new computational routine is implemented within Ansys Fluent™ with the help of User-Defined Functions. Phase change data for hydrogen and methane from recent cryo-neutron experiments is compared to computational results to correlate γ to the average evaporation molar flux, making the routine free of all tuning parameters. The coefficient-free model is validated using additional experimental data. Errors in the evaporation rate are found to be less than 5%.

1. Introduction

Liquid–vapor phase change is a fundamental phenomenon in countless natural and engineering processes, such as in new energy infrastructure on Earth and in space. Of pertinent interest are the growing applications of cryogenic fuels, which require reliable storage and transportation technologies with minimal boil-off [1–4]. However, a complete and accurate understanding of evaporation has eluded us for centuries [5], in large part due to the multi-scale, multi-physics nature of phase change processes. Evaporation from a single-species liquid phase to a multi-species vapor phase is limited by the diffusion rate of the evaporating molecules through the vapor phase, described by Fick's law [6–8]. On the other hand, evaporation between the liquid and vapor phases of the same species is defined by the local kinetic behavior of the molecules at the interface. Popular phase change models, such as Lee's model [9], employ tuning coefficients to model the macroscopic effects of interfacial kinetic processes.

1.1. Lee's model

Lee's model [9] computes the interphase mass transfer as a function of the difference between the interface temperature and saturation

temperature,

$$S_m = \mathcal{L} \phi_v \rho_v \frac{T - T_{sat}}{T_{sat}}, \quad \text{for condensation, if } T < T_{sat}$$

$$S_m = \mathcal{L} \phi_l \rho_l \frac{T - T_{sat}}{T_{sat}}, \quad \text{for evaporation, if } T > T_{sat} \quad (1)$$

where S_m is the volumetric mass source term, ϕ is the volume fraction in the mesh cell, ρ is the density, and T and T_{sat} are the interface and saturation temperatures, respectively. Of pertinent interest is \mathcal{L} , which is both a tuning coefficient for the phase change model and a relaxation factor for the computation. A review of studies using Lee's model shows major disagreement in coefficient values. Although Lee's work set the value of \mathcal{L} to 10^{-1} s^{-1} [9], this assumption does not provide valid results for all cases. It is common for \mathcal{L} to be tuned to match experimental data [10,11] or to achieve numerical stability [12,13]. In a comprehensive review article, Kharangate and Mudawar [14] found values of \mathcal{L} ranging eight orders of magnitude from 10^{-1} to 10^7 s^{-1} , while Kim et al. [15] found coefficient values ranging nine orders of magnitude from 10^{-1} to 10^8 s^{-1} . Even lower coefficient values of $2 \times 10^{-2} \text{ s}^{-1}$ were found in the work of Wang et al. [16] and $9 \times 10^{-2} \text{ s}^{-1}$ in the work of Yang et al. [17], making the Lee coefficients

* Corresponding author.

E-mail addresses: yasinaz@mail.uc.edu (A. Yasin), bellurkn@ucmail.uc.edu (K. Bellur).

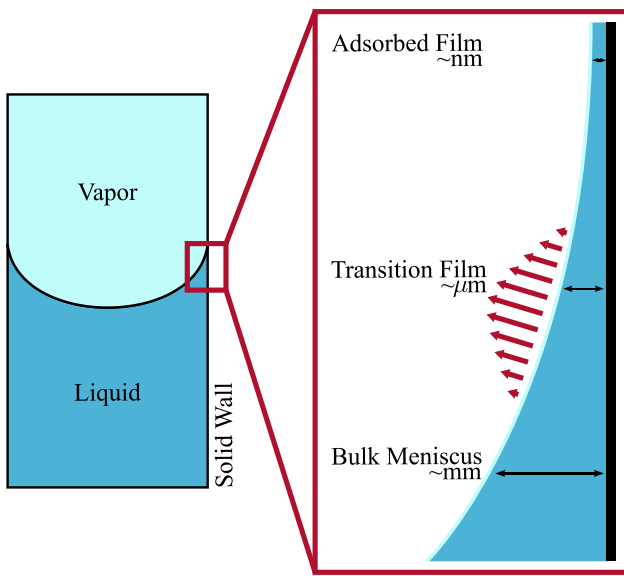


Fig. 1. Regions of a curved meniscus near a solid wall. The interface ranges from millimeter-scale in the bulk region to micrometer-scale in the transition thin film region to nanometer-scale in the adsorbed film region. The evaporation mass flux peaks in the transition scale, shown in red arrows.

range 10 orders of magnitude in literature. This disagreement in its values has made the Lee coefficient a difficult-to-predict non-physical parameter typically used to account for any physics not captured by the model.

A common approach is to use values from other studies with similar physical parameters [12]. However, there is little consistency in the coefficient values [18]. Tan et al. [12] reviewed studies where Lee's model was used to simulate thermosiphons and found values of \mathcal{L} ranging from 2×10^{-2} to 10^2 s^{-1} . Similarly, in the case of microchannels, Fang et al. [19] reported a value of 10^2 s^{-1} while Da Riva and Del Col [20] used values as high as 10^7 s^{-1} . Coefficient values are often approximated by comparing Lee's model to the Hertz–Knudsen–Schrage model (Eq. (2)) [10], of which Lee's model is understood to be a simplified form [13,14,21,22]. However, this requires values of the accommodation coefficient, α , as an input.

1.2. Kinetic theory of phase change

The Hertz–Knudsen–Schrage model [23–25] derives from the kinetic theory of gases,

$$\dot{m}'' = \frac{2}{2 - \alpha_{\text{cond}}} \sqrt{\frac{M}{2\pi\bar{R}}} \left(\alpha_{\text{evap}} \frac{P_l^{\text{sat}}}{\sqrt{T_l}} - \alpha_{\text{cond}} \frac{P_v}{\sqrt{T_v}} \right) \quad (2)$$

where \dot{m}'' is the phase change mass flux, α is the accommodation coefficient, M is the molar mass, \bar{R} is the universal gas constant, P_l^{sat} is the saturation pressure at liquid temperature, P_v is the vapor pressure, and T_l and T_v are the liquid and vapor temperatures, respectively.

The Hertz–Knudsen–Schrage model was originally developed for a planar interface, but in reality, most liquid–vapor surfaces are curved, leading to non-uniformity in thermophysical properties. Fig. 1 shows the three regions of a curved wetting meniscus in the vicinity of a solid wall. In the millimeter-scale bulk region, capillary pressure is dominant and interface curvature is mostly constant. The meniscus forms a film that eventually reaches a nanometer-scale adsorbed film region where disjoining pressure arising from intermolecular forces becomes dominant and suppresses evaporation. The micrometer-scale transition thin film region experiences an interplay of both capillary and disjoining pressures. Furthermore, thermal resistance due to conduction through the thin film reduces with film thickness. For these reasons,

the liquid–vapor interface is not anticipated to be isothermal and consequently, the mass flux is non-uniform. A maximum evaporation flux is expected in the transition film region [26–34]. To account for the effects of curvature, Wayner et al. [35,36] derived a modified version of the Hertz–Knudsen–Schrage equation using the Clapeyron and Gibbs–Duhem equations. This model was further modified by Bellur et al. [28] and presented with nondimensional terms,

$$\dot{m}'' = \left(\frac{2\alpha_{\text{cond}}}{2 - \alpha_{\text{cond}}} \right) \sqrt{\frac{M}{2\pi\bar{R}T_v}} P_v \left[\beta W \sqrt{\frac{T_v}{T_l}} - 1 \right]$$

where $W = \frac{P_v^{\text{sat}}}{P_v} + \left(1 - \frac{T_v}{T_l} \right) \left(\frac{\rho_v^{\text{sat}} h_{fg}}{P_v} \right) + \left(\frac{T_v}{T_l} \right) \left(\frac{\rho_v^{\text{sat}}}{\rho_l} \right) \left(\frac{\Pi + \sigma\kappa}{P_v} \right)$

(3)

where P_v^{sat} and ρ_v^{sat} are the saturation pressure and density at vapor temperature, respectively, h_{fg} is the enthalpy of vaporization, Π is disjoining pressure, σ is surface tension, and κ is surface curvature. The factor β is the ratio of the accommodation coefficients for evaporation and condensation, i.e., $\beta = \alpha_{\text{evap}}/\alpha_{\text{cond}}$. In this study, the evaporation and condensation coefficients are assumed to be equal, i.e., $\beta = 1$, as is common in literature [35–39], though recent works have explored their inequality [40–42]. The resulting coefficient ($\alpha = \alpha_{\text{evap}} = \alpha_{\text{cond}}$) is hereafter referred to as the accommodation coefficient. α is an essential input to all kinetic phase change models. However, nearly a century of experimental measurements of the accommodation coefficient have not found agreement [28,43]. Marek and Straub [44] reviewed decades of experimental studies of water to find reported values spanning four orders of magnitude. Despite efforts to tabulate values for various substances [39,45–47], data for countless fluids such as cryogenic fluids are severely limited [28]. As a result, computational models often reduce the accommodation coefficient to a tuning parameter to match experimental results [10,48], or assume a constant value of unity [49–56].

Although the accommodation coefficient is traditionally described as a constant [44,46,47], recent works have shown evidence of temperature dependence [27,42,57–60]. Using a combination of transition state theory and molecular dynamics simulations, Nagayama and Tsutsumi [61] derived a closed-form description of the accommodation coefficient as a function of the ratio of the liquid and vapor densities,

$$\alpha = (1 - \ell) \cdot \exp \left[\frac{-\ell}{2(1 - \ell)} \right]$$

$$\ell = \left(\frac{\rho_v}{\rho_l} \right)^{1/3} \quad (4)$$

where ρ_l and ρ_v are the liquid and vapor densities, respectively. Nagayama's model has shown good agreement with molecular dynamics data for several hydrocarbons [28,62–64] (blue points in Fig. 2(a)). Further, data from cryo-neutron experiments [65] was analyzed by Bellur et al. [28] and shows a promising match to the transition state theory (red points in Fig. 2(a)). Fig. 2(b) shows the variation of the accommodation coefficient along the saturation curve for hydrogen and methane as predicted by Nagayama's model.

Nagayama's model allows in situ calculations of the accommodation coefficient; this forms the first step towards a coefficient-free model. However, additional inputs needed for the kinetic models (Eqs. (2) and (3)) are the pressures, temperatures, and densities of the liquid and vapor phases. Of particular interest here is the vapor temperature, T_v . Kinetic models require properties obtained close to the liquid–vapor interface, typically in the Knudsen layer. However, values of T_v from a macroscale CFD grid may differ from interfacial vapor temperature. The following section discusses temperature variation in the Knudsen layer and its impact on the phase change calculation.

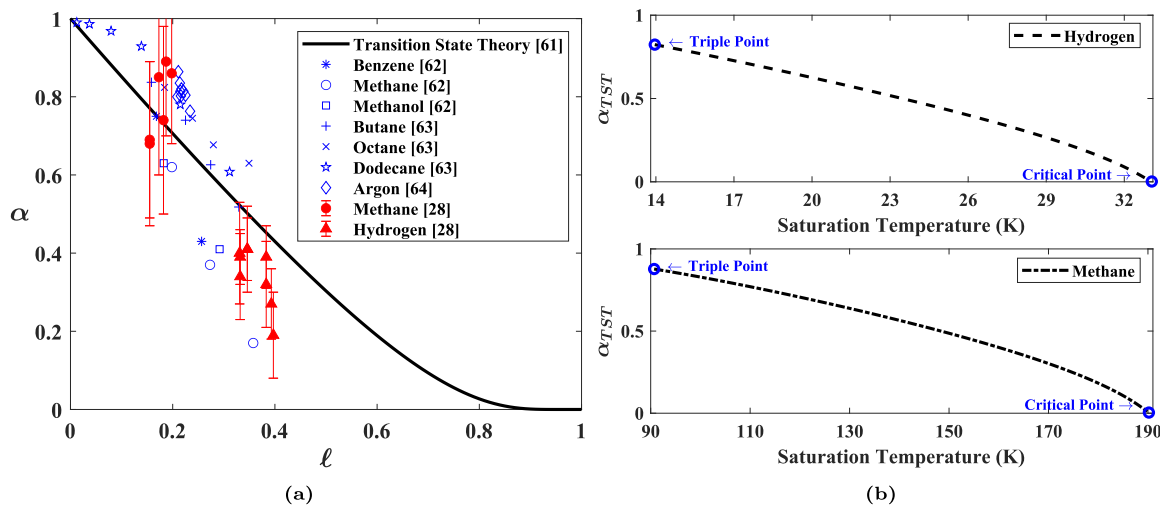


Fig. 2. (a) Correlation between recent phase change studies with hydrocarbons and the transition state theory model. Data from molecular dynamics studies are shown in blue, and data from experimental studies are shown in red. (b) Variation in the accommodation coefficient along the saturation curves of hydrogen and methane as calculated using the transition state theory model.

1.3. Gradients in vapor temperature

Temperature gradients across the interface have long been debated in the literature [43]. Liquid–vapor phase change is a non-equilibrium phenomenon where temperatures and densities across the interface are no longer continuous [64]. The non-equilibrium effects occur in a few mean paths from the interface, known as the Knudsen layer, and are perceived as temperature discontinuities at the continuum scale and have been measured experimentally [66–71]. At sub-continuum length scales, molecular dynamics studies have shown large gradients in the vapor temperature. Data for Argon reported by Liang et al. [59,72, 73] shows the temperature in the Knudsen layer (T_v^*) to be 2–3 K lower than the bulk vapor temperature (T_v) during evaporation. Akkus et al. [64] reported the inverse effect ($T_v^* > T_v$) during condensation. Recent experimental studies have probed temperatures at low continuum length scales and corroborated similar vapor temperature gradients [74]. Polikarpov et al. [75] found the Hertz–Knudsen–Schrage model to overpredict phase change rates if vapor temperatures are taken from outside the Knudsen layer; however, good agreement with experimental results was shown if vapor temperatures were taken from the upper boundary of the Knudsen layer. Currently, this overprediction is suppressed by using unrealistically low values of the accommodation coefficient. No models exist to relate the temperature gradients to the phase change rates, posing a challenge for continuum-scale models. Here, we approximate,

$$T_v^* = T_v (1 - \gamma) \quad (5)$$

where $\gamma \in [0, 1]$ is a reduction factor defined with the help of experimental data and further discussed in Section 5. After Nagayama's model, the approximation of the Knudsen layer temperature will form the second step towards a coefficient-free computational routine. The development of the computational routine is described in the following section.

1.4. Present study

In this study, we aim to address the issues inherent in almost all popular phase change models and develop a physics-based computational model of evaporation that does not require tuning coefficients. The modified kinetic phase change model for curved interfaces developed by Bellur et al. [28] forms the basis for the computational routine. Nagayama's model is used for in situ calculations of the accommodation coefficient (α). The vapor temperature in the Knudsen layer (T_v^*) is

approximated by reducing the continuum-scale vapor temperature (T_v). This routine is detailed in Section 4.

This procedure requires values of the reduction factor (γ) to be known. Data from recent cryo-neutron experiments are used to obtain values of γ for two fluids, hydrogen and methane. In the following sections, the experimental setup is recreated as a CFD domain and γ is tuned until the evaporation rates from the simulations match the experimental results. In Section 5, an expression to calculate γ as a function of the area-averaged molar flux (J_M) is derived, making the phase change calculation free of all tuning parameters. Further, the computational routine is validated using additional experimental cases, and the final computational routine is presented in Section 5.

2. Phase change experiments

Cryo-neutron phase change experiments conducted at NIST [65, 77,78] were selected to provide data to help derive values of γ and validate the coefficient-free computational routine. The cryogenic nature of these experiments provides a unique dataset of experimentally measured evaporation rates from a single species without any non-condensables in a well-controlled environment, making it an ideal case for the kinetic phase change models. The low evaporation rates and high-resolution measurements allow the setup to be modeled in a quasi-steady state, simplifying the computations. The prior work by Bellur et al. [3,79] analyzing the heat transfer and multiscale evaporation in this experimental setup further aids the use of the data for the purposes of the present study. The experiments investigated phase change in hydrogen and methane at pressures from 80–250 kPa. The experiments were motivated by a key hurdle for long-term space missions [4,80] where understanding and modeling evaporation in these cryogens is critical. Storage tanks containing these fluids undergo evaporation, resulting in boil-off and self-pressure leading to significant losses [1, 2,81–89].

The experiments used a neutron beamline to image the liquid volume of hydrogen and methane inside a cryostat during phase change (Fig. 3(a)). Evaporation or condensation was induced using a heater inside the cryostat. These images were analyzed to characterize the change in liquid volume and, therefore, the total evaporation rates [76] (Fig. 3(a)). Cylindrical test cells of aluminum (Al 6061) with diameters of 10 mm and 30 mm, and stainless steel (SS 316) with a diameter of 10 mm were used along with one conical aluminum test cell with two cylindrical sections of diameters 5 mm and 30 mm joint by a 10° angle. Fig. 3(b) shows an axisymmetric cross-section of the inside of

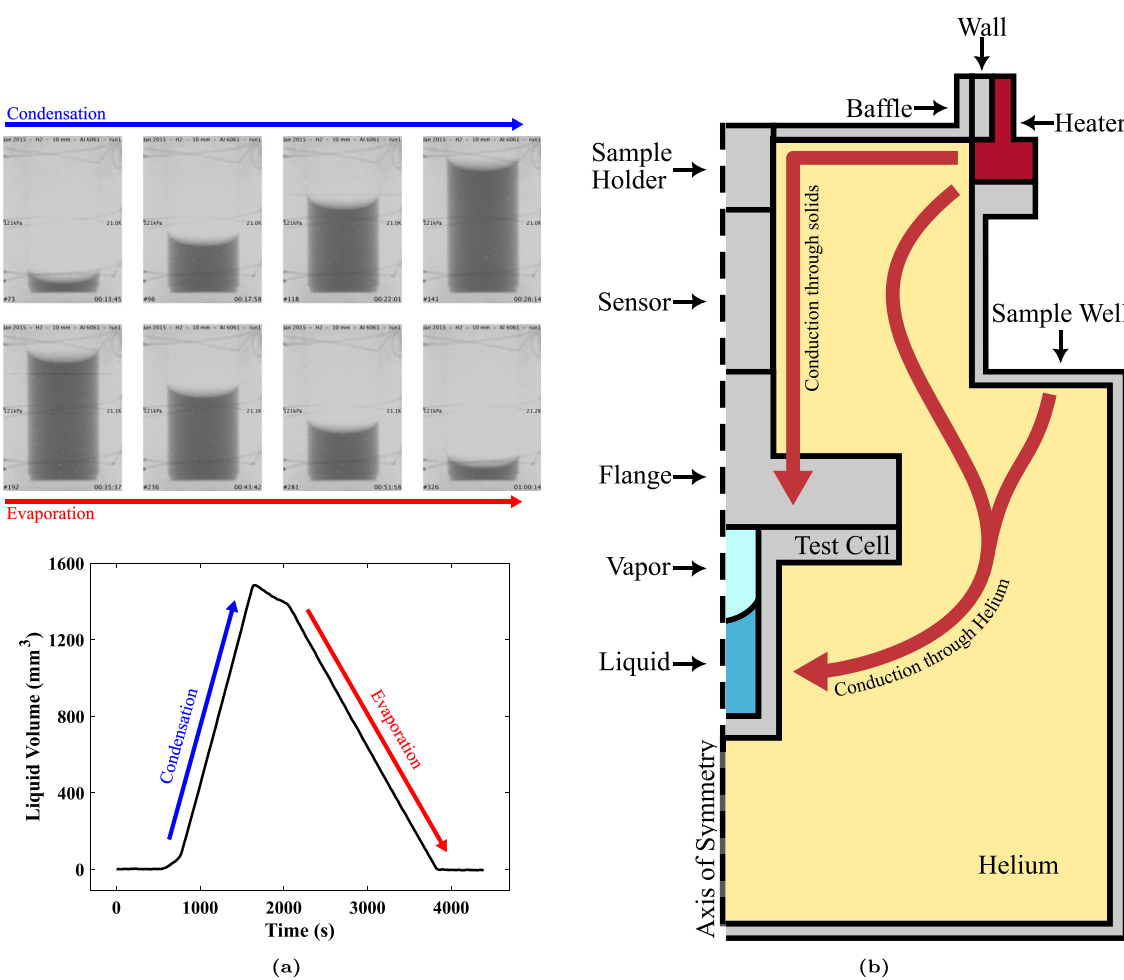


Fig. 3. (a) Selected neutron images from the hydrogen tc4 run1. Bellur et al. [76] analyzed the images to determine the liquid volume over time. (b) An axisymmetric depiction of the inside of the cryostat. The relative placement of the solid sections, helium, and hydrogen/methane liquid and vapor are shown. This diagram is not to scale; see supplementary materials for to-scale diagrams.

the cryostat, including the test cell containing the hydrogen/methane, the helium bath, the heater, and the various solid parts. Details of the experiment are available in Ref. [78], and the supporting data can be found in the corresponding data article [65]. Data for twenty individual experimental runs are used in this study. These are divided into two random groups: (1) a *training* set of sixteen experimental runs (Table 1) that are used to develop a functional form of $\gamma(J_M)$ in Section 5 and (2) a *validation* set containing four experimental runs to validate the coefficient-free computational routine in Section 6. The following section details the CFD setup used to recreate these experimental runs.

3. CFD setup

The setup of the phase change experiments shown in Fig. 3(b) is recreated as a computational domain. Detailed drawings with dimensions and materials are provided in the supplementary material. To accurately model heat transfer through the computational domain, temperature-dependent values of specific heat and thermal conductivity of aluminum 6061 [90,91], copper [92], and stainless steel 316 [90] are used in the simulations. Quad-dominant meshes with over 2.2×10^5 mesh cells are generated for each computational domain. Mesh cell sizes range from 2 mm in the helium to 50 μm at solid–solid and fluid–solid interfaces, 20 μm at the liquid–vapor interface, and 5 μm near the contact line (Fig. 4). All simulations in this study are performed in Ansys Fluent™ using the SIMPLE-C algorithm to solve the incompressible steady-state Navier–Stokes (Eqs. (6) and (7)) and energy (Eq.

(8)) equations [10,93].

$$\nabla \cdot \vec{u} = S_m \quad (6)$$

$$\rho(\vec{u} \cdot \nabla)\vec{u} = -\nabla P + \mu\nabla^2\vec{u} + \rho\vec{g} \quad (7)$$

$$\rho\nabla \cdot (\vec{u}H) = k\nabla^2T + S_{\text{LH}} + S_{\text{HB}}, \quad \text{where } H = \int_{T_{\text{ref}}}^T c_p dT \quad (8)$$

where \vec{u} is the velocity, \vec{g} is the gravitational acceleration, c_p is the specific heat, and H is the sensible enthalpy. S_m is a mass source term used to add the evaporating mass to the phase change, S_{LH} is a heat sink term used to account for the latent heat of vaporization, and S_{HB} is used to set the temperature of the evaporating mass source to the saturation temperature of the fluid. The calculation and implementation of the source terms are detailed in the following section. The cell-based least squares scheme is used to compute gradients, and the second-order upwind scheme is used for the pressure, momentum, and energy calculations [10]. Under-relaxation factors of 0.3 and 0.7 are used for the pressure and momentum calculations, respectively. Simulations are solved until all residuals drop below 10^{-6} .

The thermal energy for evaporation is provided by the heater. Heat transfer analysis of the experimental setup performed by Bellur et al. [3] found (1) convection in the low-pressure helium gas to be negligible and (2) significant thermal contact resistance at the solid–solid interfaces, values of which were determined with the help of experimental *dry test* data. In the present study, the helium domain is modeled without convection to improve computational speeds, and

prior published values of contact resistances are used. Dry test simulations to validate the heat transfer through the computational domain are described in Yasin's MS thesis [94], along with grid sensitivity for the computational domain.

Due to the highly wetting nature of their liquid phases, hydrogen and methane form menisci with high curvature, meeting the walls of the cylindrical test cells at low contact angles [95]. The contact angles and menisci shapes were experimentally determined by Bellur et al. [79,96] and shown to agree with solutions to the Young–Laplace equation for static menisci in right circular cylinders derived by Concus [97],

$$\left. \begin{aligned} \frac{d\bar{h}(\psi)}{d\psi} &= \frac{\sin \psi}{Bo \cdot \bar{h} - (\sin \psi)/\bar{r} + \lambda} \\ \frac{d\bar{r}(\psi)}{d\psi} &= \frac{\cos \psi}{Bo \cdot \bar{h} - (\sin \psi)/\bar{r} + \lambda} \end{aligned} \right\} \quad (0 < \psi < \frac{\pi}{2} - \theta) \quad (9)$$

where \bar{h} is the dimensionless height of the meniscus at dimensionless radial position \bar{r} , Bo is the dimensionless Bond number, θ is the contact angle, λ is a parameter that is twice the curvature at the apex of the meniscus, and $\psi = \tan^{-1}(d\bar{h}/d\bar{r})$. Here, the meniscus shape is obtained by numerically solving the system of ODEs using a variable-step variable-order Adams–Bashforth–Moulton solver (ode113 in MATLAB™) inside a bisection search algorithm which optimizes the value of the parameter λ in Eq. (9) until the following boundary conditions are met within an error of 10^{-9} ,

$$\bar{h}(\psi) = \bar{r}(\psi) = 0 \quad \text{at } \psi = 0 \quad (10)$$

$$\bar{r}(\psi) = 1 \quad \text{at } \psi = \pi/2 - \theta \quad (11)$$

However, Concus's ODEs do not account for the effects of disjoining pressure, and as a result, the meniscus shape becomes inaccurate in the transition thin film region [79]. This region also suffers from ill-conditioned computational meshes due to the rapidly decreasing distance between the meniscus and the solid wall [29]. Therefore, a *cutoff* is introduced by truncating the curved meniscus at a distance of 10 μm away from the solid wall (Fig. 4(b)). All physical phenomena below this length scale are ignored in the present study. Bellur et al. [79] estimated that the region below 10 μm contributes 5%–22% of the total evaporation rate, depending on the size of the test cell.

A mesh size of 50 μm is used in the fluid domains and at the fluid–solid interfaces. A structured mesh is created along the liquid–vapor interface with quadrilateral mesh cells of 20 μm and further refined near the cutoff region to a size of 5 μm. The mesh cells along the liquid–vapor interface are structured such that each mesh cell on one side of the interface corresponds to a cell on the other side. This single-cell layer on either side of the interface is identified as the *active region* (Fig. 4(c)). The use of the active region mesh allows for interfacial fluid properties to be obtained from the CFD solution and be used as inputs to the phase change model. Evaporating mass is added to the vapor active region and allowed to flow out of the pressure outlet (Fig. 4(a)). No mass is removed from the liquid domain. This simplification allows for the setup to be modeled in a quasi-steady state, where the interface position is held fixed at an experimentally determined position and is justified due to (1) low evaporation rates and (2) negligible change in the meniscus shape [76]. The quasi-steady state approach reduces the overall computation and allows the simulation results to be compared to instantaneous data from the experiments. Evaporation is implemented in the active region mesh using source terms (Eqs. (6) and (8)) computed by the computational routine discussed in the following section.

4. Computational routine

Source terms allow heat and mass to be added or removed from specific mesh cells in the active region. To allow for spatial variation in

the evaporation mass flux along the length of the meniscus, the routine is executed for each mesh cell pair along the meniscus at every iteration of the CFD solver. Therefore, a refined and structured interfacial mesh, as described in the previous section, is necessary to obtain local fluid properties and compute the local evaporation mass flux. Fig. 5 shows such a mesh refinement where active region cells on opposite sides of the interface are coupled to form *mesh cell pairs*.

Algorithm 1 Phase change algorithm with reduction factor, γ , as an input.

Require: $\gamma \in [0, 1]$, molar mass, M , enthalpy of vaporization, h_{fg} , and universal gas constant, \bar{R} as inputs.

for each mesh cell pair in the *active region* **do**

(1) Query liquid and vapor properties for the current mesh cell pair: P_v , T_v , T_l , ρ_l and ρ_v from the current iteration of the CFD solution, and face area, A_{cell} , volume, V_{cell} , and curvature, κ from the mesh data.

(2) Calculate saturation properties P_v^{sat} , ρ_v^{sat} , and specific heat, c_p as polynomial functions of T_v , surface tension, σ , as a polynomial function of T_l , and disjoining pressure, Π using Equation (13).

(3) Calculate the accommodation coefficient, α , using ρ_v and ρ_l as inputs to Equation (4).

(4) Approximate Knudsen layer vapor temperature, T_v^* , using γ and T_v as inputs to Equation (5).

(5) Calculate the phase change mass flux, \dot{m}'' , using T_v^* and other required inputs to Equation (3).

(6) Calculate the latent heat flux, \dot{Q}_{LH}'' , using \dot{m}'' and h_{fg} as inputs to Equation (14).

(7) Calculate the volumetric mass source term, S_m , using \dot{m}'' , A_{cell} , and V_{cell} as inputs to Equation (15).

(8) Calculate the latent heat source term, S_{LH} , using \dot{Q}_{LH}'' , A_{cell} , and V_{cell} as inputs to Equation (16).

(9) Calculate the heat balance source term, S_{HB} , using S_m , T^{sat} , and c_p as inputs to Equation (17), where T^{sat} is the saturation temperature at P_v .

(10) Return source terms S_m , S_{LH} , and S_{HB} to the CFD solver.
end for

The computational routine is summarized in Algorithm 1. It requires a value of γ and experimentally measured temperature and meniscus location data as inputs along with physical constants, such as molar mass, M , enthalpy of vaporization, h_{fg} , and the universal gas constant, R . In step (1), the liquid and vapor properties for the current mesh cell pair are queried from the CFD solver, properties of the mesh cells are read from mesh data, and interface curvature, κ , is obtained from pre-calculated values, which are tabulated for the meniscus shape using a well-known 2D formulation for cylindrical geometries [98,99],

$$\kappa = \frac{h''}{(1 + h'^2)^{\frac{3}{2}}} + \frac{1}{(R - h)(1 + h'^2)^{\frac{1}{2}}} \quad (12)$$

where $h = h(x)$ is the distance between the meniscus and solid wall, x is the distance along the axis of the cylinder, and R is the radius of the cylinder. In step (2), saturation pressure, P_v^{sat} , density, ρ_v^{sat} , and specific heat, c_p of the vapor phase, and surface tension, σ , are calculated using polynomial curve fits of data from the NIST Standard Reference Database [100]. Disjoining pressure is modeled using,

$$\Pi = \frac{\mathcal{A}}{h^3} \quad (13)$$

where \mathcal{A} is the Hamaker constant [101]. In step (3), the value of the accommodation coefficient is calculated using Nagayama's model. In step (4), the continuum-scale vapor temperature, T_v , obtained from the CFD solution in step (1) is reduced by a factor γ to approximate the temperature in the Knudsen layer, T_v^* as discussed in Section 1.3. In step (5), T_v^* is used to calculate the phase change mass flux, \dot{m}'' . In step

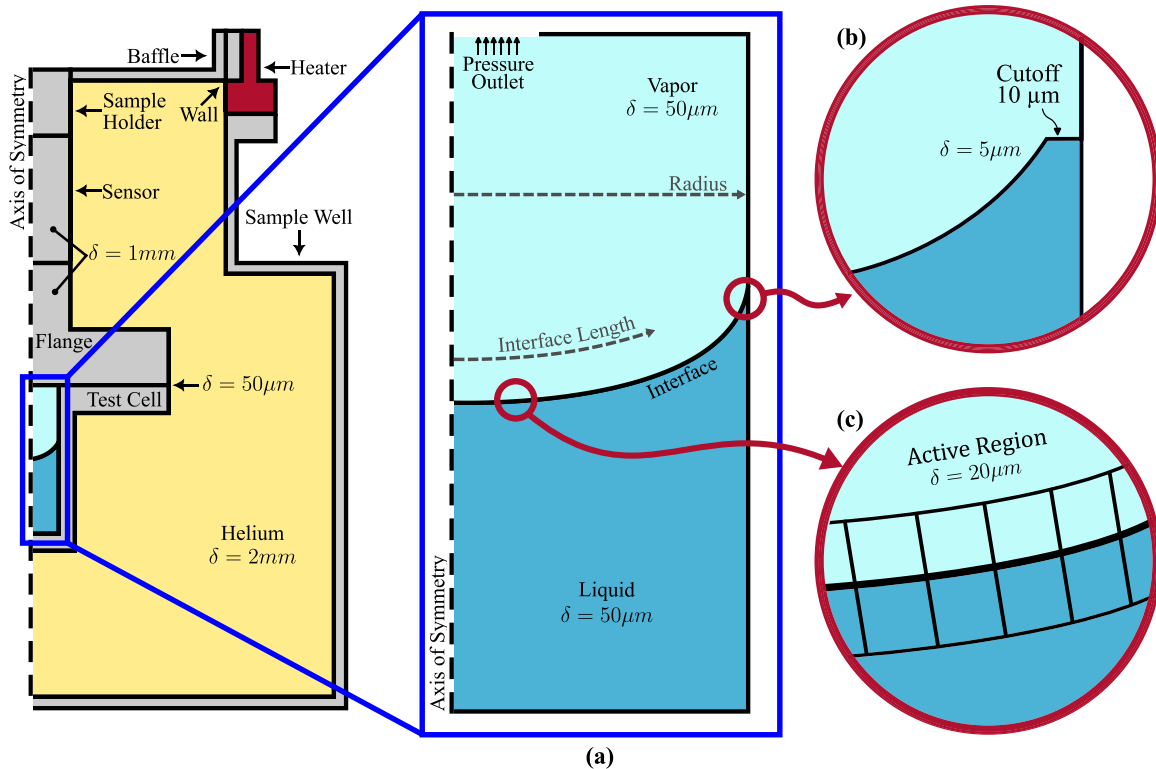


Fig. 4. Important features of the computational domain are shown. Approximate mesh sizes in a region are shown as values of δ . (a) The inside of the test cell contains the liquid and vapor domains separated by a curved interface. The top of the vapor domain includes a pressure outlet. (b) The meniscus is terminated at a distance of $10 \mu\text{m}$ away from the wall, creating an artificial *cutoff* region. (c) A single layer of mesh cells on either side of the interface is marked as the *active region*. The active region mesh is structured such that each cell in the liquid active region is paired with a corresponding cell in the vapor active region. Phase change-related sources and sinks are computed and applied locally for each cell pair.

(6), the latent heat loss corresponding to the evaporation mass flux is calculated,

$$\dot{Q}_{\text{LH}}'' = -\dot{m}'' \cdot h_{\text{fg}} \quad (14)$$

where h_{fg} is the latent heat of vaporization of the evaporating species. In steps (7) and (8), the evaporation mass flux and the latent heat loss are converted to volumetric mass and heat source terms, S_m and S_{LH} respectively,

$$S_m = \dot{m}'' \times \frac{A_{\text{cell}}}{V_{\text{cell}}} \quad (15)$$

$$S_{\text{LH}} = \dot{Q}_{\text{LH}}'' \times \frac{A_{\text{cell}}}{V_{\text{cell}}} \quad (16)$$

where A_{cell} is the mesh cell face area adjacent to the interface and V_{cell} is the cell volume (Fig. 5). Ansys Fluent™ introduces mass sources at a reference temperature, T_{ref} , of 298.15 K [10] (Eq. (8)). However, the evaporating mass must enter the vapor phase at a temperature close to the saturation temperature. A heat balance source term, S_{HB} , is used to account for this temperature difference and is calculated in step (9) as,

$$S_{\text{HB}} = -S_m \cdot c_p \cdot (T_{\text{ref}} - T_{\text{sat}}) \quad (17)$$

where c_p is the specific heat of the vapor phase and T_{sat} is the saturation temperature.

Finally, in step (10), the three source terms, S_m , S_{LH} , and S_{HB} , are returned to the CFD solver to be applied to the vapor cell. This adds the evaporating mass to the vapor cell at saturation temperature while removing the associated latent heat of vaporization. The routine is implemented in Ansys Fluent™ with the help of four User-Defined Functions (UDFs) to extract liquid properties from the liquid active region and calculate the three source terms in the vapor active region. The UDFs allow the source terms to be computed for each mesh cell

pair along the interface at each iteration of the CFD solver, coupling the phase change calculations with the CFD computation. The routine described in this section is implemented within the CFD setup described in Section 3 to recreate the phase change experiments. The following section discusses the results obtained from these simulations.

5. Results and discussion

Using Algorithm 1 and the CFD setup described in Section 3, sixteen experimental runs, shown in Table 1 are simulated. Values of the accommodation coefficient, α , are calculated *in situ* and allowed to evolve in each simulation. This method is found to be numerically stable and converges to residuals of 10^{-6} within 10^3 iterations of the CFD solver, after which results are extracted (Fig. 7). In this section, interfacial temperature and mass flux data obtained from the CFD simulations are presented, and the comparison of computational and experimental data is described. Interfacial data is presented along the normalized interface length, defined as the ratio of the distance along the meniscus to the radius of the cylindrical container (Fig. 4(a)).

Liquid and vapor temperatures increase from the apex of the meniscus to the cutoff region, as is expected due to the conductive heat transfer from the wall of the test cell (Fig. 6(a)). Similarly, the evaporation mass flux is found to increase from the apex to the cutoff but suddenly reduces because contributions of the transition thin film are not modeled (Fig. 6(b)). A similar mass flux distribution was found by the multiscale analysis performed by Bellur et al. [79] where vapor properties were assumed constant.

The contributions of capillary and disjoining pressures on the phase change rate were found to be several orders of magnitude smaller than the thermal contributions because of the near-constant bulk curvature and relatively large distance between the interface and the container

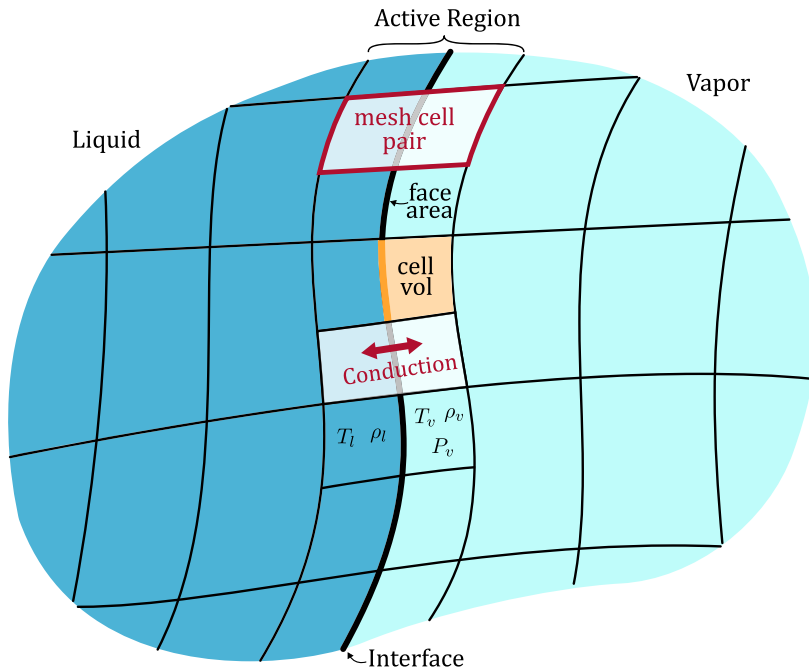


Fig. 5. The refined mesh near the liquid–vapor interface is shown. A single-cell layer on either side is identified as the active region. Active region mesh cell pairs are made of corresponding liquid and vapor cells. The interface is modeled as a wall in Ansys Fluent™, allowing conductive heat transfer but no mass transfer across it. Source terms are computed using the field variables from the active region, which are queried at the cell centroids of each mesh cell pair. Mass and heat fluxes are converted to volumetric source terms using the cell volume and face area.

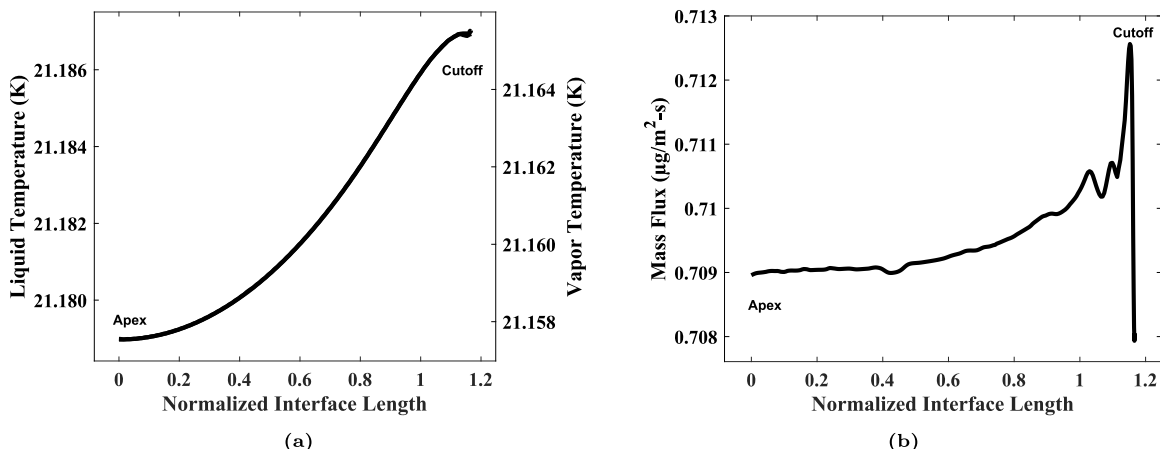


Fig. 6. Interfacial properties during evaporation in hydrogen (tc4 run1). The horizontal axis ranges from the apex of the meniscus at the center of the cylindrical test cell to the wall of the test cell. (a) Liquid and vapor temperatures increase along the interface length and are greater than $T_{\text{sat}} = 20.99$ K. (b) Evaporation mass flux is obtained by using $\gamma = 10^{-3}$ in Eq. (4). Integrating the mass flux distribution over the interfacial surface area gives a total evaporation rate of 55.4 $\mu\text{g}/\text{s}$.

wall in the bulk meniscus region modeled in this study. The local evaporation mass flux is found to be sensitive to the interfacial temperatures, T_l and T_v^* . Liquid active region temperature, T_l , is found to be greater than both vapor temperatures, T_v and T_v^* , but their difference is never greater than 1 K (i.e., $T_l - T_v^* < 1$ K). To compare the computational and experimental results, the interfacial mass flux is numerically integrated over the liquid surface to obtain a total evaporation rate,

$$\dot{m} = \iint_{A_{\text{surf}}} \dot{m}'' dA \approx \sum_{i=1}^N \dot{m}_i'' \pi (r_{i+1}^2 - r_i^2) \quad (18)$$

where \dot{m} is the evaporation rate, \dot{m}'' is the mass flux, A_{surf} is the interfacial surface, dA is an area element of the surface, r is the distance along the test cell radius, and N is the number of active region mesh cells along the meniscus from the apex to the contact line.

Initially, the reduction factor, γ , is tuned to match experimental evaporation rates within an error of 1%. Values of γ obtained from this

process are listed in Table 1 and shown in Fig. 8(a). Although γ appears to be a linear function of \dot{m} , its slope depends on the evaporating fluid (hydrogen or methane) and the size of the test cell, shown as different trendlines in Fig. 8(a). Data for additional fluids is needed to fully understand the dependency of γ and the evaporating fluid. The need for γ as an input to Algorithm 1 requires γ to be tuned to match experimental data. The ability to predict values of γ would make the computational routine free of all tuning parameters. A universal function to calculate γ requires eliminating fluid and geometry dependencies. To achieve this, we scale the evaporation rate, \dot{m} , by the molar mass, M , (to remove the influence of the evaporating fluid) and by the surface area of the liquid–vapor interface, A_{surf} , (to remove the effects of the test cell size), leading to the area-averaged molar flux,

$$J_M = \frac{\dot{m}}{M \times A_{\text{surf}}} \quad (19)$$

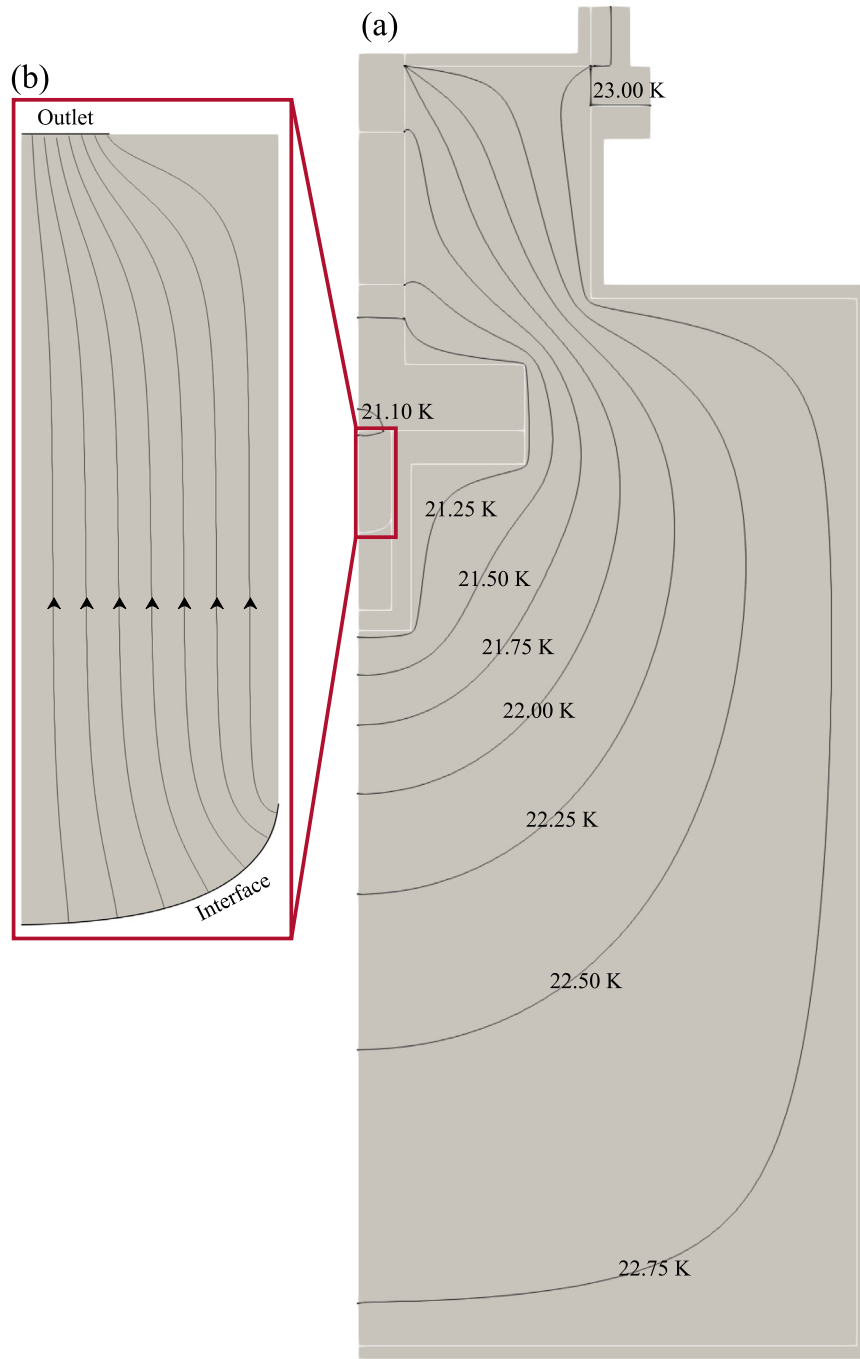


Fig. 7. CFD results of evaporation in hydrogen (tc4 run1). (a) Contour plot of the temperature distribution in the domain. (b) Streamlines in the vapor phase are shown.

Fig. 8(b) shows values of γ as a function of the area-averaged molar flux J_M and all the data points collapse into a single curve. Since γ represents the physical decrease in interfacial temperature due to the non-equilibrium effects of evaporation, it is expected that $\gamma \rightarrow 0$ as $J_M \rightarrow 0$ and γ is finite and bounded as $J_M \rightarrow \infty$. Therefore, an exponential curve fit is used to define a smooth function to calculate γ ,

$$\gamma = c_1 \{ \exp(c_2 \cdot J_M) - 1 \}, \quad \text{where, } c_1 = -3.1370 \times 10^{-3}, \\ c_2 = -9.9679 \times 10^{-1} \quad (20)$$

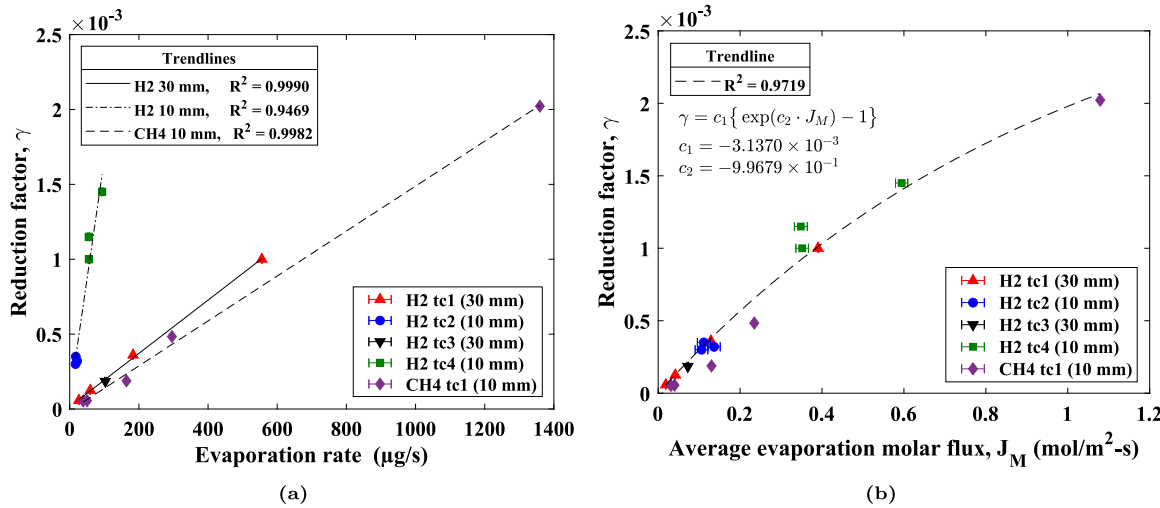
Eq. (20) allows γ to be calculated *in situ* as a function of J_M , instead of being tuned. Coupling Eq. (20) with the kinetic mass flux model (Eq. (3)) within the computational routine will allow γ and m'' to be calculated *in-situ* without the need for tunable inputs. Algorithm 2 shows

the modified computational routine, where Eqs. (3) and (20) are solved iteratively, eliminating the need for all tuning parameters (steps 4 and 5). This new tuning parameter-free method is validated using additional experimental runs, detailed in the following section. Major sources of uncertainty in this method include the experimental uncertainty in the measurements of the evaporation rates [65,76], shown as error bars in Fig. 8. Additionally, contributions of the transition thin film region to the evaporation rate are not modeled in this study; previously estimated to be 5%–22% of the total evaporation rate using a multiscale model with guessed values of the accommodation coefficient [79].

The size of the interfacial mesh cells was varied to understand the dependency of the phase change calculation on the mesh size. Reducing the interfacial mesh size reduces the temperature jump across the interface, which in turn leads to reduced evaporation. However,

Table 1Values of the reduction factor, γ , for the different experimental cases.

Fluid	Test cell No.	Test cell	Run No.	Saturation temperature (K)	Evaporation rate ($\mu\text{g/s}$)	Reduction factor, γ
H_2	tc1	30 mm Al	2	21.0	552.93	1.00×10^{-3}
			3	19.9	59.02	1.25×10^{-4}
			4	19.9	183.99	3.60×10^{-4}
			6	21.6	26.72	5.80×10^{-5}
H_2	tc2	10 mm SS	1	21.0	16.93	3.00×10^{-4}
			2	19.9	17.27	3.50×10^{-4}
			3	23.0	21.40	3.20×10^{-4}
H_2	tc3	30 mm Al	1	21.0	103.71	1.85×10^{-4}
H_2	tc4	10 mm Al	1	21.0	54.67	1.00×10^{-3}
			2	19.9	54.95	1.15×10^{-3}
			3	23.0	91.71	1.45×10^{-3}
CH_4	tc1	10 mm Al	1	121.0	164.03	1.88×10^{-4}
			2	115.4	1359.61	2.00×10^{-3}
			3	111.9	295.61	4.84×10^{-4}
			4	116.8	39.01	5.40×10^{-5}
			5	121.0	50.21	5.54×10^{-5}

Fig. 8. Values of the reduction factor, γ from Table 1 as a function of (a) the total evaporation rate, and (b) the area-averaged molar flux.

the value of γ remains consistent since the temperature gradient is unchanged. The lack of a thin film model is more apparent when the mesh size is reduced, and a cut-off length appropriate for the mesh size needs to be picked. The observed variation in the evaporation rate is within the expected contribution from the thin film.

6. Validation

Four randomly chosen experimental runs were preserved to serve as a validation dataset and are shown in Table 2. This data was not a part of the original set used to develop $\gamma(J_M)$ so it serves as a unique data subset to validate the non-tuning computational routine given by Algorithm 2. The CFD setup described in Section 3 is used along with the same UDFs to implement Algorithm 2 in Ansys Fluent. A tolerance of 10^{-10} is used for step (5). Fig. 9 shows the spatial distribution of evaporation mass flux and reduction factor, γ , obtained using this method. Since Eq. (20) is derived using a spatially invariant value of γ ; therefore, the distribution of γ obtained from Algorithm 2 must be spatially averaged. This is done by using an averaged value of γ from the prior iteration as an input to compute the local mass flux in the next iteration. This method preserves the numerical stability and yields a framework where no tuning or input coefficients are needed. The only input needed is $\gamma(J_M)$, which is shown to be both material and geometry

independent. Table 2 compares total evaporation rates obtained using this procedure with the experimental data, showing good agreement in all cases (<5% error). However, the error tends to increase as the test cell size reduces. This is explained by the higher fraction of transition thin film evaporation in the smaller test cells. Bellur et al. [79] analyzed the relative contributions of the different regions of the interface to the total evaporation rate and reported the transition thin film contributions to be two to four times higher in the 10 mm test cells than the 30 mm test cells matching the trend seen in Table 2.

7. Summary and conclusion

Popular models of liquid-vapor phase change, such as the Lee model, rely heavily on tuning coefficients to compute the evaporating mass transfer. A review of recent literature shows values of the Lee coefficient spanning ten orders of magnitude, with little agreement in coefficient values between similar studies. This makes the Lee coefficient hard to predict and the model difficult to implement. On the other hand, kinetic theory-based phase change models require values of the accommodation coefficient as input. Although the accommodation coefficient is a physics-based parameter, experimental data from close to a century of studies provide values spanning three orders of magnitude for water, while little data exists for cryogenic fluids.

Table 2

Comparison of results from the non-tuning algorithm and experimental data.

Fluid	Test cell No.	Test cell	Run No.	Saturation temperature (K)	Experimental evaporation rate ($\mu\text{g/s}$)	Modeled evaporation rate ($\mu\text{g/s}$)	Relative error
H_2	tc1	30 mm Al	1	21.0	234.69	237.93	1.38%
			8	22.5	885.75	882.65	0.35%
H_2	tc2	10 mm SS	5	23.0	76.74	73.09	4.76%
H_2	tc4	10 mm Al	4	23.0	76.41	79.67	4.27%

Algorithm 2 Non-tuning phase change algorithm.

Require: Molar mass, M , enthalpy of vaporization, h_{fg} , and universal gas constant, \bar{R} as inputs.

for each mesh cell pair in the active region do

(1) Query liquid and vapor properties for the current mesh cell pair: P_v , T_v , T_l , ρ_l and ρ_v from the current iteration of the CFD solution, and face area, A_{cell} , volume, V_{cell} , and curvature, κ from the mesh data.

(2) Calculate saturation properties P_v^{sat} , ρ_v^{sat} , and specific heat, c_p as polynomial functions of T_v , surface tension, σ , as a polynomial function of T_l , and disjoining pressure, Π using Equation (13).

(3) Calculate the accommodation coefficient, α , using ρ_v and ρ_l as inputs to Equation (4).

(4) Set an initial value for γ and calculate T_v^* using γ and T_v as inputs to Equation (5).

(5) Iterate between Equation (3) to calculate the phase change mass flux, m'' , Equation (19) & (20) to calculate γ , and Equation (5) to calculate T_v^* until m'' converges to a desired tolerance.

(6) Calculate the latent heat flux, \dot{Q}_{LH}'' , using m'' and h_{fg} as inputs to Equation (14).

(7) Calculate the volumetric mass source term, S_m , using m'' , A_{cell} , and V_{cell} as inputs to Equation (15).

(8) Calculate the latent heat source term, S_{LH} , using \dot{Q}_{LH}'' , A_{cell} , and V_{cell} as inputs to Equation (16).

(9) Calculate the heat balance source term, S_{HB} , using S_m , T^{sat} , and c_p as inputs to Equation (17), where T^{sat} is the saturation temperature at P_v .

(10) Return source terms S_m , S_{LH} , and S_{HB} to the CFD solver.
end for

Transition State Theory expression (Eq. (4)). The vapor Knudsen layer temperature, T_v^* , is approximated by reducing the macroscopic vapor temperature, T_v , by a fraction γ . The values of α and T_v^* , along with other thermophysical properties, are used as inputs to the kinetic phase change model (Eq. (3)) to calculate the local evaporation mass flux, m'' . Source terms to simulate the evaporating mass transfer entering at saturation temperature and the latent heat loss are calculated and implemented on the vapor side of the interface.

With the help of the computational routine, CFD simulations are used to recreate phase change experiments in Ansys Fluent™. User-Defined Functions are used to implement the routine in Ansys Fluent™. Values of the reduction factor, γ , are obtained by tuning γ until the resulting evaporation rate matches the experimental data within 1% relative error. Values of γ obtained from this process are found to be a strong function of the area-averaged molar flux, J_M . The function (Eq. (20)) forms a system of equations with the kinetic model (Eq. (3)) that allows γ and the evaporation mass flux to be calculated simultaneously within the computational routine. The computational routine is modified (Algorithm 2) to solve Eqs. (3) and (20) to m'' and γ along the interface.

A two-step process is introduced where the distribution of γ from Algorithm 2 are spatially averaged and used as an input to Algorithm 1. Four new random experimental runs are used to validate this process. Computed phase change rates show excellent agreement with the experimental measurements with relative errors below 5%. Higher errors are observed in smaller (10 mm) test cell cases, while the larger (30 mm) test cell cases produce relative errors below 1%.

The computational routine developed in this study models evaporation mass and heat transfer in CFD setups without any tuning parameters. The model is derived using data for hydrogen and methane but offers a framework for the method to be expanded to other species and multiscale menisci. Conclusions from the study are summarized:

- Using Transition State Theory allows for *in-situ* calculation of the accommodation coefficient and provides a basis for a numerically stable tuning-free phase change model.
- Kinetic phase change models are found to be sensitive to the temperature of the vapor phase. Variations of a few percent in T_v can cause deviations of an order of magnitude in the evaporation mass flux.
- Approximating the temperature in the vapor Knudsen layer using γ greatly improves the accuracy of the model while allowing for spatial variations in the evaporation mass flux.
- The use of the area-averaged molar flux and γ suggest the method is independent of interface size, container material, and fluid.
- The errors in the total evaporation rate obtained using this method are within 5% of experimental measurements, significantly lower than the errors typically seen with tunable models.

CRediT authorship contribution statement

Ayzaaz Yasin: Investigation, Formal analysis, Methodology, Writing – original draft. **Kishan Bellur:** Conceptualization, Funding acquisition, Project administration, Supervision, Writing – review & editing.

Declaration of competing interest

The authors declare that they have no known competing financial interests or personal relationships that could have appeared to influence the work reported in this paper.

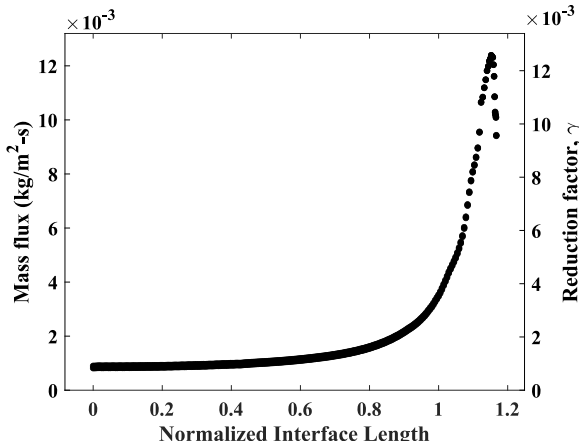


Fig. 9. Spatially varying mass flux and γ for the hydrogen tc4 run4 case obtained using the Algorithm 2.

In this study, a novel approach to modeling evaporation without tuning coefficients is presented. A new computational routine is developed and implemented within traditional CFD setups. Values of the accommodation coefficients are calculated *in-situ* using local thermophysical properties queried from the CFD solver as inputs to a

Acknowledgments

The authors thank Jeffrey Allen at the Michigan Technological University for insightful and constructive feedback. This work was supported by the NSF CAREER Award (#CBET2339757). The authors acknowledge support from the University of Cincinnati through a Graduate Incentive Award for Ayaaz Yasin.

Appendix A. Supplementary data

Supplementary material related to this article can be found online at <https://doi.org/10.1016/j.aplthermaleng.2025.126807>.

Data availability

Data will be made available on request.

References

- [1] J.W. Hartwig, Liquid acquisition devices for advanced in-space cryogenic propulsion systems, 2014.
- [2] J.D. Clark, Ignition! An Informal History of Liquid Rocket Propellants, Rutgers University Press, New Brunswick, N.J., ISBN: 978-0-8135-0725-5, 1972.
- [3] K. Bellur, E. Médici, J. Hermanson, C. Choi, J. Allen, Determining solid-fluid interface temperature distribution during phase change of cryogenic propellants using transient thermal modeling, *Cryogenics* 91 (2018) 103–111, <http://dx.doi.org/10.1016/j.cryogenics.2018.02.009>, ISSN 00112275.
- [4] N.R. Council, NASA Space Technology Roadmaps and Priorities: Restoring NASA's Technological Edge and Paving the Way for a New Era in Space, National Academies Press, Washington, D.C., ISBN: 978-0-309-25362-8, 2012, p. 13354, <http://dx.doi.org/10.17226/13354>.
- [5] W. Brutsaert, Evaporation into the atmosphere: Theory, history, and applications, Environmental Fluid Mechanics, Hingham, MA, Dordrecht, Holland ; Boston, ISBN: 978-90-277-1247-9, 1982, Reidel; Sold and distributed in the U.S.A. and Canada by Kluwer Boston.
- [6] D. Spalding, The combustion of liquid fuels, *Symp. (Int.) Combust.* 4 (1) (1953) 847–864, [http://dx.doi.org/10.1016/S0082-0784\(53\)80110-4](http://dx.doi.org/10.1016/S0082-0784(53)80110-4), ISSN 00820784.
- [7] A.P. Pinheiro, J.M. Vedovoto, Evaluation of droplet evaporation models and the incorporation of natural convection effects, *Flow Turbul. Combust.* 102 (3) (2019) 537–558, <http://dx.doi.org/10.1007/s10494-018-9973-8>, ISSN 1386-6184, 1573-1987.
- [8] A. Saufi, R. Calabria, F. Chiariello, A. Frassoldati, A. Cuoci, T. Faravelli, P. Massoli, An experimental and CFD modeling study of suspended droplets evaporation in buoyancy driven convection, *Chem. Eng. J.* 375 (2019) 122006, <http://dx.doi.org/10.1016/j.cej.2019.122006>, ISSN 13858947.
- [9] W.H. Lee, Pressure iteration scheme for two-phase flow modeling, Technical Report la- UR 79- 975, 1979, pp. 407–431.
- [10] Ansys Fluent 12.0/12.1 Documentation.
- [11] B. Li, X. Wang, Y. Man, B. Li, W. Wang, Numerical simulation method for flash evaporation with circulating water based on a modified lee model, *Energies* 16 (21) (2023) 7453, <http://dx.doi.org/10.3390/en16217453>, ISSN 1996-1073.
- [12] Z. Tan, Z. Cao, W. Chu, Q. Wang, Improvement on evaporation-condensation prediction of lee model via a temperature deviation based dynamic correction on evaporation coefficient, *Case Stud. Therm. Eng.* 48 (2023) 103147, <http://dx.doi.org/10.1016/j.csite.2023.103147>, ISSN 2214157X.
- [13] H. Liu, J. Tang, L. Sun, Z. Mo, G. Xie, An assessment and analysis of phase change models for the simulation of vapor bubble condensation, *Int. J. Heat Mass Transfer* 157 (2020) 119924, <http://dx.doi.org/10.1016/j.ijheatmasstransfer.2020.119924>, ISSN 0017-9310.
- [14] C.R. Kharangate, I. Mudawar, Review of computational studies on boiling and condensation, *Int. J. Heat Mass Transfer* 108 (2017) 1164–1196, <http://dx.doi.org/10.1016/j.ijheatmasstransfer.2016.12.065>, ISSN 0017-9310.
- [15] D.G. Kim, C.H. Jeon, I.S. Park, Comparison of numerical phase-change models through stefan vaporizing problem, *Int. Commun. Heat Mass Transfer* 87 (2017) 228–236, <http://dx.doi.org/10.1016/j.icheatmasstransfer.2017.07.013>, ISSN 0735-1933.
- [16] X. Wang, H. Yao, J. Li, Y. Wang, Y. Zhu, Experimental and numerical investigation on heat transfer characteristics of ammonia thermosyphons at shallow geothermal temperature, *Int. J. Heat Mass Transfer* 136 (2019) 1147–1159, <http://dx.doi.org/10.1016/j.ijheatmasstransfer.2019.03.080>, ISSN 0017-9310.
- [17] Z. Yang, X.F. Peng, P. Ye, Numerical and experimental investigation of two phase flow during boiling in a coiled tube, *Int. J. Heat Mass Transfer* 51 (5) (2008) 1003–1016, <http://dx.doi.org/10.1016/j.ijheatmasstransfer.2007.05.025>, ISSN 0017-9310.
- [18] H. Lee, C.R. Kharangate, N. Mascarenhas, I. Park, I. Mudawar, Experimental and computational investigation of vertical downflow condensation, *Int. J. Heat Mass Transfer* 85 (2015) 865–879, <http://dx.doi.org/10.1016/j.ijheatmasstransfer.2015.02.037>, ISSN 0017-9310.
- [19] C. Fang, M. David, A. Rogacs, K. Goodson, Volume of fluid simulation of boiling two-phase flow in a vapor-venting microchannel, *Front. Heat Mass Transf.* 1 (1) (2010) <http://dx.doi.org/10.5098/hmt.v1.3002>, ISSN 2151-8629.
- [20] E. Da Riva, D. Del Col, Effect of gravity during condensation of r134a in a circular minichannel, *Microgravity Sci. Technol.* 23 (1) (2011) 87–97, <http://dx.doi.org/10.1007/s12217-011-9275-4>, ISSN 1875-0494.
- [21] M. Bahreini, A. Ramiar, A.A. Ranjbar, Numerical simulation of bubble behavior in subcooled flow boiling under velocity and temperature gradient, *Nucl. Eng. Des.* 293 (2015) 238–248, <http://dx.doi.org/10.1016/j.nucengdes.2015.08.004>, ISSN 00295493.
- [22] S.C. De Schepper, G.J. Heynderickx, G.B. Marin, Modeling the evaporation of a hydrocarbon feedstock in the convection section of a steam cracker, *Comput. Chem. Eng.* 33 (1) (2009) 122–132, <http://dx.doi.org/10.1016/j.compchemeng.2008.07.013>, ISSN 00981354.
- [23] H. Hertz, Ueber die Verdunstung der Flüssigkeiten, insbesondere des Quecksilbers, im luftleeren raume, *Ann. Phys., Lpz.* 253 (10) (1882) 177–193, <http://dx.doi.org/10.1002/andp.18822531002>, ISSN 00033804, 15213889.
- [24] M. Knudsen, Die maximale verdampfungsgeschwindigkeit des quecksilbers, *Ann. Phys., Lpz.* 352 (13) (1915) 697–708, <http://dx.doi.org/10.1002/andp.19153521306>, ISSN 00033804, 15213889.
- [25] R. Schrage, A Theoretical Study of Interphase Mass Transfer (Ph.D. thesis), Columbia University Press, 1953.
- [26] P.G.D. Gennes, X. Hua, P. Levinson, Dynamics of wetting: Local contact angles, *J. Fluid Mech.* 212 (1990) 55–63, <http://dx.doi.org/10.1017/S0022112090001859>, ISSN 1469-7645, 0022-1120.
- [27] E. Lakew, A. Sarchami, G. Giustini, H. Kim, K. Bellur, Thin film evaporation modeling of the Liquid Microlayer Region in a dewetting water bubble, *Fluids* 8 (4) (2023) 126, <http://dx.doi.org/10.3390/fluids8040126>, ISSN 2311-5521.
- [28] K. Bellur, E.F. Médici, J.C. Hermanson, C.K. Choi, J.S. Allen, Modeling liquid-Vapor phase change experiments: cryogenic hydrogen and methane, *Colloids Surf. A: Physicochem. Eng. Asp.* 675 (2023) 131932, <http://dx.doi.org/10.1016/j.colsurfa.2023.131932>, ISSN 09277757.
- [29] U. Chakrabarti, A. Yasin, K. Bellur, J.S. Allen, An investigation of phase change induced marangoni-dominated flow patterns using the constrained vapor bubble data from ISS experiments, *Front. Space Technol.* 4 (2023) <http://dx.doi.org/10.3389/frst.2023.1263496>, ISSN 2673-5075.
- [30] A.M. Abolmaali, M. Bayat, J. Hattel, A multiscale analytical-numerical method for the coupled heat and mass transfer in the Extended Meniscus Region considering thin-film evaporation in microchannels, *Int. J. Heat Mass Transfer* 222 (2024) 125145, <http://dx.doi.org/10.1016/j.ijheatmasstransfer.2023.125145>, ISSN 00179310.
- [31] J.L. Plawsky, S.S. Panchamgam, S.J. Gokhale, P.C. Wayner, S. DasGupta, A study of the oscillating corner meniscus in a vertical constrained vapor bubble system, *Superlattices Microstruct.* 35 (3–6) (2004) 559–572, <http://dx.doi.org/10.1016/j.spmi.2003.11.010>, ISSN 07496036.
- [32] T.T. Nguyen, J. Yu, J.L. Plawsky, P.C. Wayner, D.F. Chao, R.J. Sicker, Spontaneously oscillating menisci: maximizing evaporative heat transfer by inducing condensation, *Int. J. Therm. Sci.* 128 (2018) 137–148, <http://dx.doi.org/10.1016/j.ijthermalsci.2018.02.015>, ISSN 12900729.
- [33] L. Zheng, J.L. Plawsky, P.C. Wayner Jr., S. DasGupta, Stability and oscillations in an evaporating corner meniscus, *J. Heat Transf.* 126 (2) (2004) 169–178, <http://dx.doi.org/10.1115/1.1652046>, ISSN 0022-1481.
- [34] G. Preiss, P.C. Wayner Jr., Evaporation from a capillary tube, *J. Heat Transf.* 98 (2) (1976) 178–181, <http://dx.doi.org/10.1115/1.3450515>, ISSN 0022-1481.
- [35] P. Wayner, Y. Kao, L. LaCroix, The interline heat-transfer coefficient of an evaporating wetting film, *Int. J. Heat Mass Transfer* 19 (5) (1976) 487–492, [http://dx.doi.org/10.1016/0017-9310\(76\)90161-7](http://dx.doi.org/10.1016/0017-9310(76)90161-7), ISSN 00179310.
- [36] P.C. Wayner, The effect of interfacial mass transport on flow in thin liquid films, *Colloids Surf.* 52 (1991) 71–84, [http://dx.doi.org/10.1016/0166-6622\(91\)80006-A](http://dx.doi.org/10.1016/0166-6622(91)80006-A), ISSN 01666622.
- [37] C.-Y. Zhao, L.-W. Liang, L.-Y. Yang, F.-F. Zhang, A. Karmakar, D. Qi, J.-M. Jiang, C.N. Markides, Modelling of evaporative falling-film heat transfer over a horizontal tube, *Appl. Therm. Eng.* 255 (2024) 123997, <http://dx.doi.org/10.1016/j.aplthermaleng.2024.123997>, ISSN 1359-4311.
- [38] S. DasGupta, I.Y. Kim, P.C. Wayner, Use of the kelvin-clapeyron equation to model an evaporating curved microfilm, *J. Heat Transf.* 116 (4) (1994) 1007–1015, <http://dx.doi.org/10.1115/1.2911436>, ISSN 0022-1481, 1528-8943.
- [39] P. Davidovits, C.E. Kolb, L.R. Williams, J.T. Jayne, D.R. Worsnop, Update 1 of: mass accommodation and chemical reactions at gas-liquid interfaces, *Chem. Rev.* 111 (4) (2011) cr100360b, <http://dx.doi.org/10.1021/cr100360b>, ISSN 0009-2665, 1520-6890.
- [40] U. Chakrabarti, K. Bellur, J.S. Allen, Investigating the inequality of phase change coefficients using ISS experimental data, *Nanoscale Microscale Thermophys. Eng.* (2025) submitted for publication.

- [41] K. Montazeri, S. Hao, M.J. Abdolhosseini Qomi, Y. Won, Molecular dynamics investigation of liquid and vapor interactions near an evaporating interface: a theoretical genetics perspective, *Adv. Theory Simul.* 3 (7) (2020) 2000017, <http://dx.doi.org/10.1002/adts.202000017>, ISSN 2513-0390, 2513-0390.
- [42] G. Chen, On the molecular picture and interfacial temperature discontinuity during evaporation and condensation, *Int. J. Heat Mass Transfer* 191 (2022) 122845, <http://dx.doi.org/10.1016/j.ijheatmasstransfer.2022.122845>, ISSN 0017-9310.
- [43] A.H. Persad, C.A. Ward, Expressions for the evaporation and condensation coefficients in the Hertz-Knudsen Relation, *Chem. Rev.* 116 (14) (2016) 7727–7767, <http://dx.doi.org/10.1021/acs.chemrev.5b00511>, ISSN 0009-2665, 1520-6890.
- [44] R. Marek, J. Straub, Analysis of the evaporation coefficient and the condensation coefficient of water, *Int. J. Heat Mass Transfer* 44 (1) (2001) 39–53, [http://dx.doi.org/10.1016/S0017-9310\(00\)00086-7](http://dx.doi.org/10.1016/S0017-9310(00)00086-7), ISSN 00179310.
- [45] E. Davis, A history and state-of-the-art of accommodation coefficients, *Atmos. Res.* 82 (3–4) (2006) 561–578, <http://dx.doi.org/10.1016/j.atmosres.2006.02.013>, ISSN 01698095.
- [46] B. Paul, Compilation of evaporation coefficients, *ARS J.* 32 (9) (1962) 1321–1328, <http://dx.doi.org/10.2514/8.6277>, ISSN 1936-9972.
- [47] I. Eames, N. Marr, H. Sabir, The evaporation coefficient of water: A review, *Int. J. Heat Mass Transfer* 40 (12) (1997) 2963–2973, [http://dx.doi.org/10.1016/S0017-9310\(96\)00339-0](http://dx.doi.org/10.1016/S0017-9310(96)00339-0), ISSN 00179310.
- [48] C.-Y. Chou, *Tuning Capillary Evaporation in Nanoporous Membranes: Fundamentals and Applications* (Ph.D. thesis), Boston University, United States – Massachusetts, ISBN: 9798381407402, 2024.
- [49] S.-Y. Du, Y.-H. Zhao, New boundary conditions for the evaporating thin-film model in a rectangular micro channel, *Int. J. Heat Mass Transfer* 54 (15–16) (2011) 3694–3701, <http://dx.doi.org/10.1016/j.ijheatmasstransfer.2011.02.059>, ISSN 00179310.
- [50] S.-Y. Du, Y.-H. Zhao, Numerical study of conjugated heat transfer in evaporating thin-films near the contact line, *Int. J. Heat Mass Transfer* 55 (1–3) (2012) 61–68, <http://dx.doi.org/10.1016/j.ijheatmasstransfer.2011.08.039>, ISSN 00179310.
- [51] W. Qu, T. Ma, J. Miao, J. Wang, Effects of radius and heat transfer on the profile of evaporating thin liquid film and meniscus in capillary tubes, *Int. J. Heat Mass Transfer* 45 (9) (2002) 1879–1887, [http://dx.doi.org/10.1016/S0017-9310\(01\)00296-4](http://dx.doi.org/10.1016/S0017-9310(01)00296-4), ISSN 00179310.
- [52] H. Wang, S.V. Garimella, J.Y. Murthy, Characteristics of an evaporating thin film in a microchannel, *Int. J. Heat Mass Transfer* 50 (19–20) (2007) 3933–3942, <http://dx.doi.org/10.1016/j.ijheatmasstransfer.2007.01.052>, ISSN 00179310.
- [53] H. Wang, S.V. Garimella, J.Y. Murthy, An analytical solution for the total heat transfer in the thin-film region of an evaporating meniscus, *Int. J. Heat Mass Transfer* 51 (25–26) (2008) 6317–6322, <http://dx.doi.org/10.1016/j.ijheatmasstransfer.2008.06.011>, ISSN 00179310.
- [54] S.-K. Wee, K.D. Kihm, K.P. Hallinan, Effects of the liquid polarity and the wall slip on the heat and mass transport characteristics of the micro-scale evaporating transition film, *Int. J. Heat Mass Transfer* 48 (2) (2005) 265–278, <http://dx.doi.org/10.1016/j.ijheatmasstransfer.2004.08.021>, ISSN 00179310.
- [55] S.-K. Wee, K.D. Kihm, D.M. Pratt, J.S. Allen, Microscale heat and mass transport of evaporating thin film of binary mixture, *J. Thermophys. Heat Transfer* 20 (2) (2006) 320–326, <http://dx.doi.org/10.2514/1.15784>, ISSN 0887-8722, 1533-6808.
- [56] M. Stewart, Pressurization of a lightweight, liquid hydrogen tank: evaporation & condensation at the liquid/vapor interface, in: 53rd AIAA/SAE/ASEE Joint Propulsion Conference, American Institute of Aeronautics and Astronautics, Atlanta, GA, ISBN: 978-1-62410-511-1, 2017, <http://dx.doi.org/10.2514/6.2017-4916>.
- [57] S. Cheng, J.B. Lechman, S.J. Plimpton, G.S. Grest, Evaporation of Lennard-Jones fluids, *J. Chem. Phys.* 134 (22) (2011) 224704, <http://dx.doi.org/10.1063/1.3595260>, ISSN 0021-9606, 1089-7690.
- [58] T. Ishiyama, T. Yano, S. Fujikawa, Molecular dynamics study of kinetic boundary condition at an interface between argon vapor and its condensed phase, *Phys. Fluids* 16 (8) (2004) 2899–2906, <http://dx.doi.org/10.1063/1.1763936>, ISSN 1070-6631, 1089-7666.
- [59] Z. Liang, T. Biben, P. Kebinski, Molecular simulation of steady-state evaporation and condensation: validity of the schrage relationships, *Int. J. Heat Mass Transfer* 114 (2017) 105–114, <http://dx.doi.org/10.1016/j.ijheatmasstransfer.2017.06.025>, ISSN 00179310.
- [60] T. Tsuruta, G. Nagayama, Molecular dynamics studies on the condensation coefficient of water, *J. Phys. Chem. B* 108 (5) (2004) 1736–1743, <http://dx.doi.org/10.1021/jp035885q>, ISSN 1520-6106, 1520-5207.
- [61] G. Nagayama, T. Tsuruta, A general expression for the condensation coefficient based on transition state theory and molecular dynamics simulation, *J. Chem. Phys.* 118 (3) (2003) 1392–1399, <http://dx.doi.org/10.1063/1.1528192>.
- [62] P.L. Barclay, J.R. Lukes, Curvature dependence of the mass accommodation coefficient, *Langmuir* 35 (18) (2019) 6196–6202, <http://dx.doi.org/10.1021/acs.langmuir.9b00537>, ISSN 0743-7463, 1520-5827.
- [63] G. Nagayama, M. Takematsu, H. Mizuguchi, T. Tsuruta, Molecular dynamics study on condensation/evaporation coefficients of chain molecules at liquid–vapor interface, *J. Chem. Phys.* 143 (2015) 014706.
- [64] Y. Akkus, A.T. Gurer, K. Bellur, Drifting mass accommodation coefficients: In situ measurements from a steady state molecular dynamics setup, *Nanoscale Microscale Thermophys. Eng.* 25 (1) (2020) 25–45, <http://dx.doi.org/10.1080/15567265.2020.1861139>, ISSN 1556-7265.
- [65] K. Bellur, E.F. Medici, D.S. Hussey, D.L. Jacobson, J. LaManna, J.B. Leao, J. Scherschligt, J.C. Hermanson, C.K. Choi, J.S. Allen, Data from cryo-neutron phase change experiments with LH₂ and LCH₄, *Data Brief* 43 (2022) 108474, <http://dx.doi.org/10.1016/j.dib.2022.108474>, ISSN 23523409.
- [66] E.Y. Gatapova, I.A. Graur, O.A. Kabov, V.M. Aniskin, M.A. Filipenko, F. Sharipov, L. Tadrist, The temperature jump at water – air interface during evaporation, *Int. J. Heat Mass Transfer* 104 (2017) 800–812, <http://dx.doi.org/10.1016/j.ijheatmasstransfer.2016.08.111>, ISSN 0017-9310.
- [67] F. Duan, C.A. Ward, V.K. Badam, F. Durst, Role of molecular phonons and interfacial-temperature discontinuities in water evaporation, *Phys. Rev. E* 78 (4) (2008) 041130, <http://dx.doi.org/10.1103/PhysRevE.78.041130>.
- [68] V. Badam, V. Kumar, F. Durst, K. Danov, Experimental and theoretical investigations on interfacial temperature jumps during evaporation, *Exp. Therm. Fluid Sci.* 32 (1) (2007) 276–292, <http://dx.doi.org/10.1016/j.expthermflusci.2007.04.006>, ISSN 08941777.
- [69] C.A. Ward, F. Duan, Turbulent transition of thermocapillary flow induced by water evaporation, *Phys. Rev. E* 69 (5) (2004) 056308, <http://dx.doi.org/10.1103/PhysRevE.69.056308>.
- [70] C.A. Ward, D. Stanga, Interfacial conditions during evaporation or condensation of water, *Phys. Rev. E* 64 (5) (2001) 051509, <http://dx.doi.org/10.1103/PhysRevE.64.051509>.
- [71] G. Fang, C.A. Ward, Temperature measured close to the interface of an evaporating liquid, *Phys. Rev. E* 59 (1) (1999) 417–428, <http://dx.doi.org/10.1103/PhysRevE.59.417>.
- [72] Z. Liang, P. Kebinski, Molecular simulation of steady-state evaporation and condensation in the presence of a non-condensable gas, *J. Chem. Phys.* 148 (6) (2018) 064708, <http://dx.doi.org/10.1063/1.5020095>, ISSN 0021-9606, 1089-7690.
- [73] Z. Liang, A. Chandra, E. Bird, P. Kebinski, A molecular dynamics study of transient evaporation and condensation, *Int. J. Heat Mass Transfer* 149 (2020) 119152, <http://dx.doi.org/10.1016/j.ijheatmasstransfer.2019.119152>, ISSN 00179310.
- [74] E.Y. Gatapova, Evaporation into half-space: experiments with water at the molecular mean free path scale, *Phys. Fluids* 36 (9) (2024) 091707, <http://dx.doi.org/10.1063/5.0228893>, ISSN 1070-6631.
- [75] A.P. Polikarpov, I.A. Graur, E.Y. Gatapova, O.A. Kabov, Kinetic simulation of the non-equilibrium effects at the liquid-vapor interface, *Int. J. Heat Mass Transfer* 136 (2019) 449–456, <http://dx.doi.org/10.1016/j.ijheatmasstransfer.2019.02.100>, ISSN 00179310.
- [76] K. Bellur, V. Konduru, E.F. Medici, D.S. Hussey, D.L. Jacobson, J.M. LaManna, J.S. Allen, C.K. Choi, Visualization of the evaporation and condensation phenomena in cryogenic propellants, *J. Flow Vis. Image Process.* 23 (1–2) (2016) <http://dx.doi.org/10.1615/JFlowVisImageProc.2017020115>, ISSN 1065-3090, 1940-4336.
- [77] K. Bellur, E. Médici, M. Kulshreshtha, V. Konduru, D. Tyrewala, A. Tamilarasan, J. McQuillen, J. Leão, D. Hussey, D. Jacobson, J. Scherschligt, J. Hermanson, C. Choi, J. Allen, A new experiment for investigating evaporation and condensation of cryogenic propellants, *Cryogenics* 74 (2016) 131–137, <http://dx.doi.org/10.1016/j.cryogenics.2015.10.016>, ISSN 00112275.
- [78] K. Bellur, E. Médici, D.S. Hussey, D.L. Jacobson, J. LaManna, J.B. Leão, J. Scherschligt, J.C. Hermanson, C.K. Choi, J.S. Allen, Results from neutron imaging phase change experiments with LH₂ and LCH₄, *Cryogenics* 125 (2022) 103517, <http://dx.doi.org/10.1016/j.cryogenics.2022.103517>, ISSN 00112275.
- [79] K. Bellur, E.F. Médici, C.K. Choi, J.C. Hermanson, J.S. Allen, Multiscale approach to model steady meniscus evaporation in a wetting fluid, *Phys. Rev. Fluids* 5 (2) (2020) 024001, <http://dx.doi.org/10.1103/PhysRevFluids.5.024001>.
- [80] F. Ghaffari-Tabrizi, J. Haemisch, D. Lindner, Reducing hydrogen boil-off losses during fuelling by pre-cooling cryogenic tank, *Hydrogen* 3 (2) (2022) 255–269, <http://dx.doi.org/10.3390/hydrogen3020015>, ISSN 2673-4141.
- [81] D.W. Plachta, R.J. Christie, E. Carlberg, J.R. Feller, J.G. Weisend, J. Barclay, S. Breon, J. Demko, M. DiPirro, J.P. Kelley, P. Kittel, A. Klebaner, A. Zeller, M. Zagarola, S. Van Sciver, A. Rowe, J. Pfotenhauer, T. Peterson, J. Lock, Cryogenic propellant boil-off reduction system, in: AIP Conference Proceedings, Vol. 985, AIP, Chattanooga (Tennessee), 2008, pp. 1457–1466, <http://dx.doi.org/10.1063/1.2908506>, ISSN 0094243X.
- [82] C.H. Panzarella, M. Kassemi, Self-pressure of large spherical cryogenic tanks in space, *J. Spacecr. Rockets* 42 (2) (2005) 299–308, <http://dx.doi.org/10.2514/1.4571>, ISSN 0022-4650, 1533-6794.
- [83] S. Barsi, M. Kassemi, C. Panzarella, J. Alexander, A tank self-pressure experiment using a model fluid in normal gravity, in: 43rd AIAA Aerospace Sciences Meeting and Exhibit, American Institute of Aeronautics and Astronautics, Reno, Nevada, ISBN: 978-1-62410-064-2, 2005, <http://dx.doi.org/10.2514/6.2005-1143>.

- [84] S. Barsi, M. Kassemi, Numerical and experimental comparisons of the self-pressurization behavior of an LH₂ tank in normal gravity, *Cryogenics* 48 (3–4) (2008) 122–129, <http://dx.doi.org/10.1016/j.cryogenics.2008.01.003>, ISSN 00112275.
- [85] M.M. Hasan, C.S. Lin, N.T. Vandresar, *Self-pressurization of a lightweight liquid hydrogen storage tank subjected to low heat flux*, 1991.
- [86] C. Lin, M. Hasan, Self-pressurization of a spherical liquid hydrogen storage tank in amicrogravity environment, in: 30th Aerospace Sciences Meeting and Exhibit, American Institute of Aeronautics and Astronautics, Reno, NV, U.S.A., 1992, <http://dx.doi.org/10.2514/6.1992-363>.
- [87] J.C. Aydelott, Effect of gravity on self-pressurization of spherical liquid-hydrogen tankage, 1967.
- [88] J.C. Aydelott, C.M. Spuckler, Effect of size on normal-gravity self- pressurization of spherical liquid hydrogen tankage, 1969.
- [89] M. Kassemi, O. Kartuzova, Effect of interfacial turbulence and accommodation coefficient on CFD predictions of pressurization and pressure control in cryogenic storage tank, *Cryogenics* 74 (2016) 138–153, <http://dx.doi.org/10.1016/j.cryogenics.2015.10.018>, ISSN 00112275.
- [90] D. Mann, LNG Materials and Fluids, National Bureau of Standards, Cryogenics Division, 1977.
- [91] E.D. Marquardt, J.P. Le, R. Radabaugh, Cryogenic material properties database, in: 11th International Cryocooler Conference, Keystone, CO, 2000-06-20/2000-06-22.
- [92] N.J. Simon, E.S. Drexler, R.P. Reed, Properties of copper and copper alloys at cryogenic temperatures, in: Final Report, Technical Report PB-92-172766/XAB; NIST/MONO-177, National Inst. of Standards and Technology (MSEL), Boulder, CO (United States). Materials Reliability Div., 1992, <http://dx.doi.org/10.2172/5340308>.
- [93] S.V. Patankar, *Numerical Heat Transfer and Fluid Flow*, first ed., CRC Press, Boca Raton, ISBN: 978-1-315-27513-0, 1980, <http://dx.doi.org/10.1201/9781482234213>.
- [94] A. Yasin, *Computational Modeling of Evaporation Without Tuning Coefficients* (Master's thesis), University of Cincinnati, Cincinnati, OH, 2024.
- [95] V.P. Carey, *Liquid-Vapor Phase-Change Phenomena: An Introduction to the Thermophysics of Vaporization and Condensation Processes in Heat Transfer Equipment*, Third Edition, third ed., CRC Press, Boca Raton, ISBN: 978-0-429-08222-1, 2020, <http://dx.doi.org/10.1201/9780429082221>.
- [96] K. Bellur, V. Konduру, M. Kulshrestha, D. Tyrewala, E. Medici, J.S. Allen, C.K. Choi, D.S. Hussey, D.C. Jacobson, J.B. Leão, J. McQuillen, J. Hermanson, A. Tamilarasan, Contact angle measurement of liquid hydrogen (LH₂) in stainless steel and aluminum cells, *J. Heat Transf.* 138 (2) (2016) 020904, <http://dx.doi.org/10.1115/1.4032232>, ISSN 0022-1481, 1528-8943.
- [97] P. Concus, Static Menisci in a vertical right circular cylinder, *J. Fluid Mech.* 34 (3) (1968) 481–495, <http://dx.doi.org/10.1017/S002211206800203X>, ISSN 0022-1120, 1469-7645.
- [98] A.W. Adamson, *Physical Chemistry of Surfaces*, 2. ed, Interscience Publ, New York, ISBN: 978-0-470-00793-8, 1967.
- [99] S. Hartland (Ed.), *Surface and interfacial tension: Measurement, theory, and applications*, Surfactant Science Series, (v. 119) Marcel Dekker, New York ; Basel, ISBN: 978-0-8247-5034-3, 2004.
- [100] NIST chemistry WebBook, NIST standard reference database 69, 1997, <http://dx.doi.org/10.18434/T4D303>.
- [101] J.N. Israelachvili, *Intermolecular and Surface Forces*, third ed., Elsevier Academic Press, Burlington, MA, ISBN: 978-0-12-375182-9, 2011.